American Mineralogist, Volume 100, pages 1123–1133, 2015

A photoluminescence study of REE^{3+} emissions in radiation-damaged zircon†

Christoph Lenz[1,*] and Lutz Nasdala[1]

[1]Institut für Mineralogie and Kristallographie, Universität Wien, Althanstrasse 14, 1090 Wien, Austria

Abstract

A series of natural zircon samples (with U concentrations of 140–2600 ppm and ranging from well crystalline to severely radiation damaged) were investigated by means of REE^{3+} photoluminescence spectroscopy. We found systematic changes in REE^{3+} emissions depending on the accumulated radiation damage expressed by the effective time-integrated α-dose of zircon samples. Structural reconstitution as caused by dry annealing resulted in intensity gains and decreases of half-widths of REE^{3+} emissions. The band half-widths of distinct luminescence Stark's levels of the $^4F_{9/2} \rightarrow {}^6H_{13/2}$ transition of Dy^{3+} (~17 250 cm^{-1}; ~580 nm wavelength) and the $^4F_{3/2} \rightarrow {}^4I_{9/2}$ transition of Nd^{3+} (~11 300 cm^{-1}; ~885 nm wavelength) were found to correlate sensitively with the degree of radiation damage accumulated. These REE^{3+} emissions are proposed as potential measure of the irradiation-induced structural disorder of zircon. The two emissions are considered particularly suitable because (1) they are commonly detected in PL spectra of natural zircon, and (2) they are hardly biased by other emissions or Stark's levels. Preliminary calibration curves that relate band-width increases to the α dose were established using a suite of well-characterized Sri Lankan zircon. Band broadening upon increasing corpuscular self-irradiation is assigned to increasing structural destruction, i.e., the increasing perturbation of REE^{3+} cationic lattice sites. Possible advantages of REE^{3+} luminescence spectroscopy, complementary to Raman spectroscopy, as method to quantify structural radiation damage are discussed.

Keywords: Radiation damage, rare-earth elements (REE), photoluminescence spectroscopy, hyperspectral PL mapping, zircon

Introduction

Structural disorder in U- and Th-containing minerals is caused predominantly by α-decay events, in particular comprising atomic displacements created by recoils of heavy daughter nuclei. The α particles, in constrast, have minor contribution to the total bulk damage (ca. 10–15%; Nasdala et al. 2001), whereas β and γ radiation are considered insignificant for the creation of permanent structural damage. The transformation of initially crystalline minerals into an amorphous state, through accumulation of recoil clusters over geologic periods of time, is commonly referred to as "metamictization" (e.g., Brøgger 1893; Pabst 1952; Ewing 1993).

Zircon, $ZrSiO_4$, is a widespread accessory mineral that occurs in many igneous, metamorphic, and sedimentary rocks. Zircon incorporates the actinides U^{4+} and Th^{4+} that substitute for Zr^{4+} in dodecahedral coordination (D_{2d}; Finch et al. 2001). Concentrations of the two actinides lie predominantly in the range 10–4000 ppm. As much as several weight percent have however been reported in some cases (for instance reported by Törnroos 1985; Rubin et al. 1989; Geisler et al. 2005). The accumulation of structural damage as caused by the radioactive decay of U and Th and their instable daughter nuclei, results in dramatic changes of solid-state properties. This includes changes of physical parameters such as refraction and birefringence, hardness, density, and elastic moduli (Holland and Gottfried 1955; Chakoumakos et al. 1991; Palenik et al. 2003), and a general decrease of the chemical resistance (Balan et al. 2001; Mathieu et al. 2001; Geisler et al. 2003a). The generally increased susceptibility of radiation-damaged zircon to alteration in potential post-growth processes is of enormous importance as it for instance affects negatively the ability of this mineral to immobilize radioactive elements (storage of nuclear waste; e.g., Ewing 2001) or to retain radiogenic nuclei (bias of U–Pb geochronology results; Geisler et al. 2003b).

In addition to X-ray diffraction (e.g., Weber 1990; Ríos et al. 2000), several spectroscopic techniques have been applied to quantify radiation damage accumulated in zircon. For instance, Wasilewski et al. (1973), Deliens et al. (1977), Zhang et al. (2008), and Zhang and Salje (2001) used infrared (IR) absorption spectroscopy, and Farnan and Salje (2001) and Farnan et al. (2007) applied ^{29}Si nuclear magnetic resonance (NMR) spectroscopy for the estimation of the amorphous fraction in radiation-damaged zircon. Raman spectroscopy was introduced by Nasdala et al. (1995) as a method to quantify the degree of radiation-induced structural disorder in zircon. This technique has opened up new opportunities for studying the structural state of heterogeneous zircon crystals and for investigating relationships between α-doses, age, and the annealing history of geothermal events on a micrometer-scale (cf. Nasdala et al. 2001). The present study has been performed with the objective to test the applicability of REE^{3+} luminescence spectroscopy for the very same purpose, i.e., to check if the proposed method may be used, complementary to Raman spectroscopy, to characterize and estimate non-destructively the radiation-induced disorder of zircon.

* E-mail: christoph.lenz@univie.ac.at

† Open access: Article available to all readers online.

0003-004X/15/0506–1123$05.00/DOI: http://dx.doi.org/10.2138/am-2015-4894CCBYNCND

Zircon typically incorporates traces of—mainly heavy—trivalent rare-earth elements (REE) into the structure, which is explained commonly by the coupled, xenotime-type substitution (Hanchar et al. 2001)

$$(REE^{3+},Y^{3+}) + P^{5+} \rightarrow Zr^{4+} + Si^{4+} \quad (1)$$

The emissions of REE^{3+} of zircon have been studied with different luminescence techniques based on differing excitation mechanisms, such as photoluminescence (PL, e.g., Friis et al. 2010), cathodoluminescence (CL, e.g., Blanc et al. 2000), ionoluminescence (IL, e.g., Yang et al. 1994; Finch et al. 2004), thermally induced luminescence (TL, e.g., Vaz and Senftle 1971; Van Es et al. 2002), etc. Among them, CL imaging is the most widespread technique within the Earth sciences. Intensity-based imaging of CL emissions is commonly used to visualize internal textures of zircon, which provide valuable information on primary formation and post-growth history (e.g., Vavra 1990; Hanchar and Miller 1993; Hanchar and Rudnick 1995; Rakovan and Reeder 1996; Götze 2000, 2002; Corfu et al. 2003; Götze et al. 2013). Luminescence spectroscopy of REE emissions was (and still is) used successfully to detect traces of different REE species in zircon (e.g., Nicholas 1967; Yang et al. 1992; Götze et al. 1999; Kempe et al. 2000; Gaft et al. 2001). Synthetic zircon individually or multi-doped with REEs have also been studied routinely, aiming at a better understanding of the luminescence in their natural analogs (e.g., Cesbron et al. 1995; Blanc et al. 2000; Karali et al. 2000; Hanchar et al. 2001; Friis et al. 2010).

More recently, the luminescence of REE^{3+} was used as structural probe for the characterization of REE-substituted lattice sites in minerals and mineral-based ceramics. For instance, spectral parameters of Eu^{3+} emissions have been used for the characterization of REE-substituted cation-sites in glasses and crystalline materials in process of evaluation of potential nuclear waste forms (Ollier et al. 2003; Reisfeld et al. 2004; Ternane et al. 2005).

It has been found that REE^{3+} emission-band widths are influenced significantly by the real structure, i.e., deviations from the ideal chemical composition and structural state. In particular, it has been observed that individual REE emissions broaden appreciably, and decrease in intensity, upon (1) increasing incorporation of non-formula elements (e.g., Lenz et al. 2013), and (2) increasing radiation damage (e.g., Jazmati and Townsend 2000; Nasdala et al. 2002, 2013; Ruschel et al. 2010; Panczer et al. 2012).

In the present study we review briefly the REE^{3+} photoluminescence typical of natural zircon samples, and effects of radiation damage on the REE^{3+} luminescence pattern of zircon. The potential of hyperspectral luminescence mapping, e.g., to visualize radiation damage patterns on a micrometer scale, is demonstrated by comparing well-characterized, cut zircon crystal halves (with on half annealed through heat treatment and the other left in the natural radiation-damaged state, Nasdala et al. 2006). Finally, we show that the FWHM of selected REE^{3+} luminescence sublevels of zircon is related to the amount of radiation-damage accumulated over geologic periods of time (α-dose). The latter aspect provides an alternative possibility to estimate the quantity of radiation damage present in unknown zircon samples by measuring the FWHM of REE luminescence Stark's levels.

Samples and methods

The effects of radiation damage on the REE^{3+} luminescence were first studied using four zoned samples of natural, accessory zircon single crystals (lengths ranging from 150 to 350 μm, U–Pb ages scattering between Archean and Neogene), which have been characterized in detail by Nasdala et al. (2006). In that study, single crystals were cut in two halves, along their *c*-axes. One half each was then subjected to heat treatment in air to anneal the radiation damage, whereas the other half remained in its natural, radiation-damaged state. Both, the annealed and naturally radiation-damaged half-crystal, of each sample were then embedded in epoxy, and prepared in close proximity to each other in one polished mount. These four zircon samples originated from the following lithologies and localities: (1) a potassium-rich leucogranite located near Dannemora, Adirondack Mountains, New York [sample A1; age ~1045–1050 Ma; (J.M. Hanchar and M.J. Whitehouse, personal communication); for rock description cf. McLelland et al. 2001], (2) the Bluffpoint quartz diorite, Atikwa Lawrence Batholith, Ontario [sample 81A; age 2732 ± 1 Ma; (D.W. Davis, personal communication); for rock description cf. Davis and Edwards 1985], (3) a gabbro from the Mulcahy Lake intrusion, Ontario (sample 31E; age 2733 ± 1 Ma; Morrison et al. 1985), and (4) a rhyolite tuff from the Gyulakeszi formation near Pécs, Hungary (sample M2; age 19.6 ± 1.4 Ma; Harangi 2001). An overview of the samples studied, and results of electron probe micro-analysis (EPMA), are given in Table 1 (compare also Nasdala et al. 2006).

Second, we have investigated large, homogeneous, gem-quality zircon samples. These included 13 mildly to severely radiation-damaged stones from gem gravels in the Ratnapura area, Sri Lanka (U–Pb ages in the range 522–572 Ma; Nasdala et al. 2004a, 2008), and one well-crystalline stone from the Ban Lung area, Ratanakiri, Cambodia (age 1.2 ± 0.3 Ma, P.C. Piilonen, personal communication; for sample description see Wittwer et al. 2013, and references therein). Uranium and thorium concentrations, ages, α-doses and spectroscopic data of the gem samples are listed in Table 2.

To identify specific REE^{3+} emissions in natural zircon, PL spectra of synthetic REE-doped $ZrSiO_4$ single crystals up to millimeters in size were obtained as internal references. Those materials have been synthesized in earlier studies using flux techniques; details are described elsewhere (Hanchar et al. 2001; Lenz et al. 2013).

Photoluminescence measurements in the visible to near infrared (NIR) range (single spectra and hyperspectral maps) were made using a Horiba LabRAM HR Evolution dispersive spectrometer. The spectrometer system was equipped with an Olympus BX41 optical microscope, two diffraction gratings with 600 and 1800 grooves per millimeter, and a Si-based, Peltier-cooled charge-coupled device detector. Photoluminescence was excited using a 473 nm diode-pumped solid-state laser (9 mW at the sample surface) and the 532 nm emission of a frequency-doubled Nd^{3+}:YAG laser (10 mW at the sample surface). An Olympus 100× objective (numerical aperture 0.9) was used. The system was operated in the confocal mode (confocal aperture and entrance slit set at 100 μm); the resulting lateral resolution was ~1 μm, and the depth resolution (with the beam being focused at the sample surface) was ~2–3 μm. The spectral resolution for visible light was 0.8–1.1 cm^{-1} with the 1800/mm grating (used for low-*T* measurements). The hyperspectral PL maps, consisting typically of 60 000–80 000 single spectra, were obtained using a software-controlled x–y stage. Color-coded PL maps (here, distribution patterns of the FWHM of individual Stark's levels) were then produced after appropriate data reduction, which included background correction and band-fitting assuming combined Lorentzian-Gaussian band shapes. Any mathematical correction of measured FWHMs for the system's spectral resolution (in detail discussed by Nasdala et al. 2001) turned out to be unnecessary. This is because spectrometer-related artificial broadening of Stark's level bands detected (FWHMs ≥12 cm^{-1} at room temperature) was negligibly small, owing to the high spectral resolution of the spectrometer. Low-temperature photoluminescence-measurements of homogeneous, gem-quality zircon samples were done using a long-distance, 50× objective (numerical aperture 0.55; free working distance 10.6 mm) and a Linkam FTIR-600 liquid-nitrogen cooling stage. The temperature accuracy was better than ±2 K.

Results and discussion

Photoluminescence spectra

Figure 1 shows the laser-induced (λ_{exc} = 473 nm) REE^{3+} photoluminescence spectrum of sample M2. This spectrum can be considered typical of spectra of well-crystallized natural zircon. It is dominated by groups of narrow emission bands. In contrast, broad-band yellow and blue emissions (which are more often detected in CL spectra; e.g., Götze et al. 1999) were observed

TABLE 1. Electron probe microanalysis results for cut-in-half zircon samples (data from Nasdala et al. 2006)

Zone[a]	BSE Intensity	EPMA data (wt% oxide)										
		ZrO_2	SiO_2	HfO_2	P_2O_5	Y_2O_3	Dy_2O_3	Er_2O_3	Yb_2O_3	ThO_2	UO_2	Total
Sample A1 (Adirondacks leucogranite, Fig. 3a)												
N1	middle	66.6	32.0	1.31	0.04	0.10	<0.04	0.04	<0.05	<0.02	0.04	100.1
N2	bright	66.8	32.1	1.27	<0.03	0.04	<0.04	<0.04	<0.05	<0.02	0.12	100.3
N3	very bright	65.0	31.7	0.98	0.13	0.79	0.04	0.15	0.16	0.08	0.19	99.2
A1	low	66.7	32.2	1.26	0.05	0.13	<0.04	0.04	<0.05	<0.02	0.05	100.4
A2	low	65.6	32.5	1.26	<0.03	0.03	<0.04	<0.04	<0.05	0.02	0.10	99.5
Sample 81A (Bluffpoint quartz diorite, Fig. 3b)												
N1	very bright	67.3	32.6	1.13	0.04	0.07	<0.04	0.04	<0.05	0.02	0.02	101.3
N2	middle	67.3	32.7	0.86	<0.03	0.05	<0.04	0.04	<0.05	<0.02	<0.02	100.9
N3	bright	67.1	32.6	0.81	0.05	0.17	<0.04	0.04	<0.05	<0.02	0.03	100.7
A1	low	67.1	32.6	1.11	0.03	0.06	<0.04	<0.04	<0.05	<0.02	<0.02	100.9
A2	low	67.0	32.5	0.87	0.03	0.05	<0.04	<0.04	<0.05	<0.02	<0.02	100.6
A3	low	67.0	32.6	0.84	0.06	0.17	<0.04	<0.04	<0.05	<0.02	<0.02	100.8
Sample 31E (Mulcahy Lake gabbro, Fig. 3c)												
N1	very bright	67.1	32.3	0.79	0.05	0.14	<0.04	<0.04	<0.05	<0.02	0.02	100.5
N2	low	67.6	32.3	0.54	<0.03	<0.03	<0.04	0.04	0.05	<0.02	<0.02	100.6
A1	low	67.0	32.4	0.82	0.06	0.17	<0.04	0.05	<0.05	<0.02	0.02	100.4
A2	low	66.9	32.6	0.63	<0.03	<0.03	<0.04	<0.04	<0.05	<0.02	<0.02	100.2
Sample M2 (Hungary rhyolite tuff, Fig. 4)												
N1	middle	66.7	32.8	0.96	0.27	0.11	<0.04	0.05	<0.05	<0.02	0.03	100.8
N2	very bright	65.5	32.5	1.30	0.12	0.48	0.05	0.12	0.14	0.12	0.32	100.7
A1	low	66.7	32.6	0.89	0.05	0.18	<0.04	<0.04	<0.05	<0.02	<0.02	100.6
A2	bright	65.2	32.5	1.23	0.15	0.52	0.04	0.13	0.13	0.21	0.54	100.7

Notes: Al, Ca, Fe, and Ho have also been analysed. Data are not reported here because these elements were in most cases below the detection limit of the EPMA.
[a] N = naturally, damaged un-annealed zircon sample; A = annealed zircon sample. Number after letter A or N refers to different zones of the zircon grain.

TABLE 2. Uranium and thorium concentrations, ages, α-doses, and spectroscopic data for zircon samples from Sri Lanka and Ratanakiri, Cambodia

Sample	U[a] (ppm)	Th[a] (ppm)	$^{206}Pb/^{238}U$ age[a] (Ma)	α-dose[b] ($\times10^{18}$ α/g)	effective α-dose[c] ($\times10^{18}$ α/g)	Dy^{3+} (I) FWHM (cm^{-1})	Dy^{3+} (II) FWHM (cm^{-1})	Nd^{3+} FWHM (cm^{-1})	Raman $\nu_3(SiO_4)$ FWHM[a]
M144	436 ±7	140 ± 3	552 ± 6	0.86–0.91	0.47–0.50	27.0 ± 1.4	27.0 ± 1.4	27.0 ± 2.7	7.2 ± 0.5
CZ3	550 ± 10	30 ± 2	563.9 ± 1.3	1.05–1.10	0.58–0.61	28.3 ± 1.4	27.2 ± 1.4	30.8 ± 3.1	8.2 ± 0.5
B188	556 ± 24	59 ± 4	559 ± 8	1.03–1.15	0.57–0.63	29.3 ± 1.5	27.0 ± 1.4	30.0 ± 3.4	8.5 ± 0.5
BR1	796 ± 13	39 ± 1	558 ± 13	1.47–1.60	0.81–0.88	37.5 ± 1.9	31.4 ± 1.6	34.2 ± 3.4	10.9 ± 0.8
BR231	772 ± 10	109 ± 2	571 ± 4	1.53–1.59	0.84–0.87	43.5 ± 2.2	32.4 ± 1.6	34.6 ± 3.5	11.0 ± 0.8
M257	840 ± 27	235 ± 20	561.3 ± 0.3	1.66–1.78	0.91–0.98	41.7 ± 2.1	32.8 ± 1.6	35.4 ± 3.5	11.7 ± 1.0
BR266	909 ± 17	201 ± 7	559.0 ± 0.3	1.77–1.88	0.97–1.03	44.0 ± 2.2	36.8 ± 1.8	38.0 ± 3.8	13.3 ± 1.0
M146	923 ± 17	411 ± 9	567 ± 4	1.92–2.03	1.06–1.12	47.2 ± 2.4	33.3 ± 1.7	37.0 ± 3.7	13.6 ± 1.0
M127	923 ± 23	439 ± 11	524.3 ± 0.4	1.78–1.88	0.98–1.03	50.8 ± 2.5	36.1 ± 1.8	39.7 ± 4.0	14.1 ± 1.2
OR1	1490 ± 70	279 ± 18	522 ± 3	2.62–2.92	1.44–1.61	65.2 ± 3.3	41.1 ± 2.1	42.8 ± 4.3	20.7 ± 1.5
G168	1499 ± 33	257 ± 9	547 ± 3	2.83–3.00	1.56–1.65	67.5 ± 3.4	39.6 ± 2.0	40.6 ± 4.1	24.5 ± 2.0
G4	2355 ± 84	330 ± 12	564 ± 5	4.48–4.91	2.46–2.70	81.2 ± 4.1	65.5 ± 3.3	49.6 ± 5.0	28.1 ± 2.0
G3	2572 ± 96	585 ± 34	542 ± 5	4.77–5.25	2.62–2.89	86.7 ± 4.3	67.2 ± 3.4	51.2 ± 5.1	30.4 ± 2.5
Rata	140 ± 100	90 ± 80	1.2 ± 0.3	± 0	± 0	11.8 ± 0.6	19.7 ± 1.0	14.3 ± 1.4	1.8 ± 0.3

Notes: Errors quoted are estimates that include errors of individual measurements and sample heterogeneity (scatter among multiple analyses).
[a] Sources for U and Th concentrations, ages, α-doses, and Raman-band FWHMs: Nasdala et al. (2008) for M257, Nasdala et al. (unpublished) for M127, Piilonen et al. (personal communication) and Wittwer et al. (2013) for Rata, and Nasdala et al. (2004a, and references therein) for all other samples.
[b] α-doses were calculated from U–Pb age and U and Th concentrations (Holland and Gottfried 1955; Murakami et al. 1991; Nasdala et al. 2001).
[c] Effective α-doses were estimated for zircon samples from Sri Lanka to account for incomplete damage retention by multiplying the α-dose value by a correction factor of 0.55 (for details see Nasdala et al. 2004a).

only occasionally in PL. Note that the sharpness of individual REE^{3+} emission lines (with FWHMs as small as 12 cm^{-1} at ambient temperature) may often causes confusion with Raman signals (for a detailed discussion see Nasdala et al. 2012).

Comparison of the PL spectrum of zircon M2 with spectra of synthetic REE-doped $ZrSiO_4$ (Fig. 1) reveals that the former comprises the principal transitions of traces of Dy^{3+} and Sm^{3+} in the visible to NIR spectral range. The most intense emissions are assigned to electronic transitions of Dy^{3+}, namely $^4F_{9/2} \rightarrow {}^6H_{15/2}$ near ~20 700 cm^{-1} and $^4F_{9/2} \rightarrow {}^6H_{13/2}$ near ~17 250 cm^{-1}. They are accompanied by several transitions of Sm^{3+} (Fig. 1; compare, e.g., Cesbron et al. 1995; Blanc et al. 2000; Karali et al. 2000; Gaft et al. 2001; Friis et al. 2010). In addition, low-intensity PL of Tm^{3+} and Nd^{3+} (in the NIR near ~11 400 cm^{-1}; assigned to the $^4F_{3/2} \rightarrow {}^4I_{9/2}$ transition) was observed. Assignments of electronic transitions and Russel-Saunders terms in Figure 1 have been extracted from "Dieke" energy-level diagrams (e.g., Dieke and Crosswhite 1963; Reisfeld and Jørgensen 1977; Wegh et al. 2000).

All electronic transitions detected show crystal-field splitting into sharp sublevel bands (which are commonly referred to as Stark's levels). This is caused by a non-isotropic electronegative, crystallographic environment of REE^{3+} ions (crystal field splitting; e.g., reviewed in Burns 1993). As one consequence, REE^{3+} emissions show notable orientation dependence, i.e., individual Stark's levels of a given transition may be detected with variable relative intensities, depending on crystal orientation (compare, for example, relative intensities of individual peaks in the main Dy^{3+} emissions of zircon M2 and Dy^{3+}-doped $ZrSiO_4$ in Fig. 1).

The predominance of Dy^{3+} bands in REE^{3+} luminescence spectra of natural zircon has been well documented already in CL (Mariano 1989; Rémond et al. 1992; Hanchar and Rudnick 1995; Götze et al. 1999) and IL studies (Yang et al. 1994; Finch

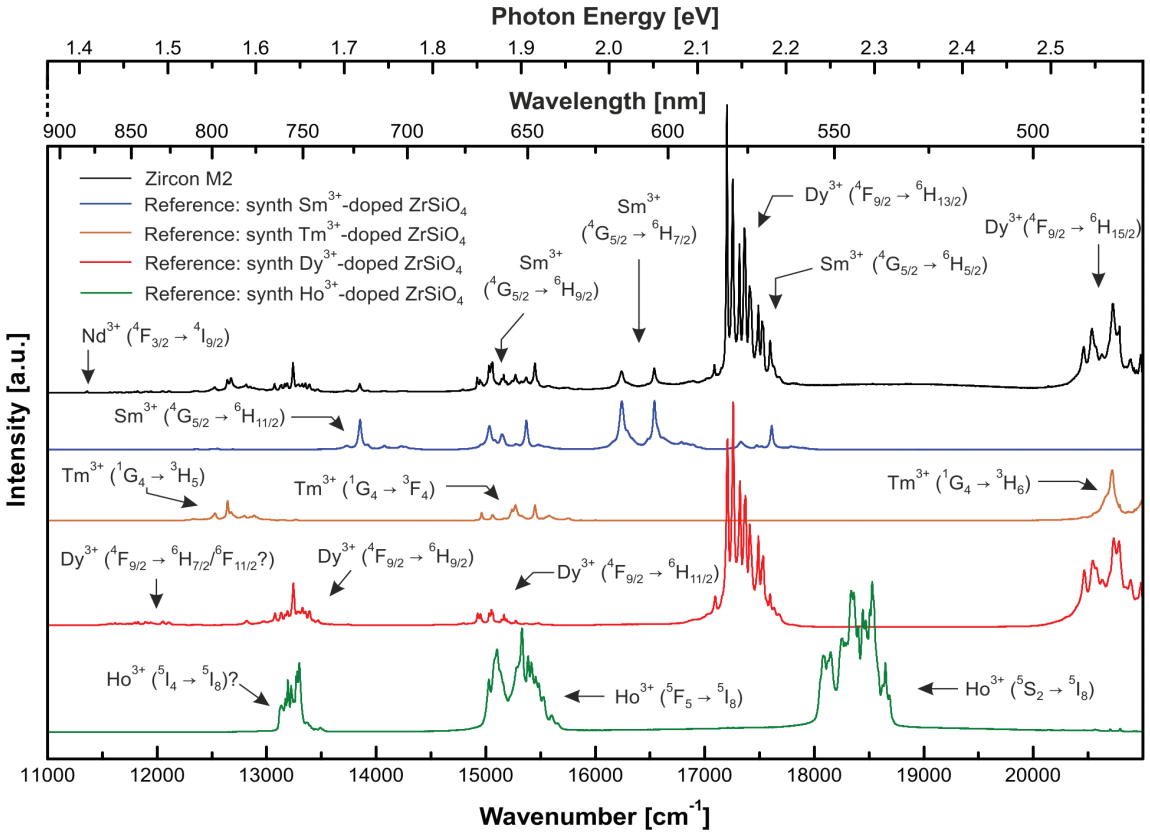

FIGURE 1. Typical laser-induced PL spectrum (λ_{exc} = 473 nm) of well-crystallized zircon in the visible to NIR spectral range (here sample M2; Pécs, Hungary). Comparison with spectra of synthetic REE-doped $ZrSiO_4$ (corresponding transitions are marked with arrows and labeled) reveals the dominance of Dy^{3+} and Sm^{3+} emissions in the natural sample, whereas the main transitions of Ho^{3+} were not observed. Minor emission signal of Nd^{3+} was observed in the NIR near ~11 400 cm^{-1}.

et al. 2004). In contrast, emissions of Ho^{3+} (cf. spectrum of Ho^{3+}-doped $ZrSiO_4$ in Fig. 1) were not detected in any steady-state PL spectrum obtained from the natural zircon samples studied here, neither with 473 nm nor with 532 nm laser-excitation. This is remarkable insofar as some of the samples have Ho and Dy concentrations of comparable magnitude. For instance, zircon M275 contains 12.6 ± 0.8 ppm Dy and 4.4 ± 0.3 ppm Ho (Nasdala et al. 2008) and M127 contains 57 ± 6 ppm Dy and 21 ± 2 ppm Ho (D. Frei, personal communication); however both samples showed intense Dy emission but no notable Ho emission bands. This observation seems to support results of the IL study of Finch et al. (2004) who concluded that Ho^{3+} emissions may be suppressed in the presence of Dy^{3+}.

Moreover, it is worthy of note that PL spectra strongly depend on the excitation wavelength. None of the PL spectra of natural zircon samples, including M257, obtained in the present study (with 473 and 532 nm laser excitation) showed emissions of Er^{3+} with significant intensity. In contrast, Er^{3+} emissions have been readily detected in PL spectra of zircon M275 obtained with 488 nm excitation (Nasdala et al. 2008). The contradiction is however only apparent, because selective excitation of REE emissions is well known in steady-state laser-induced PL (e.g., Blasse and Grabmaier 1994). Strong excitation bands of Er^{3+} centered at 490 nm ($^4I_{15/2} \rightarrow {}^4F_{7/2}$) have been reported for synthetic zircon (Friis et al. 2010). These may allow PL excitation with a nearby 488 nm, but not with a 473 nm laser.

Low-intensity emissions of Er and Ho, as well as emissions of other REEs in zircon (including Eu, Tb, Pr, Tm, Ce), which are hardly or not detectable with steady-state luminescence techniques, can however be measured using time-resolved laser-induced spectroscopy (cf. Gaft et al. 2001).

Hyperspectral PL mapping

Reliable estimation of spectral parameters (i.e., band fitting to determine FWHMs of individual REE^{3+} sublevels) is possible only if the emission detected consists of well-separated, distinct peaks. This is not the case for Sm^{3+} (and, similarly, not for Er^{3+} and Ho^{3+} emissions) in synthetic $ZrSiO_4$ whose emissions show numerous Stark's levels that strongly superimpose each other (Fig. 2A). In contrast, Stark's levels of the $^4F_{9/2} \rightarrow {}^6H_{13/2}$ transition of Dy^{3+} (especially those two in the range 17 240–17 260 cm^{-1}) can be identified and fitted without bias, as there are intense and not obscured by other bands (Fig. 2B). Dy^{3+} Stark's level I (Fig. 2B) is therefore used exemplarily in the present study, for the creation of PL maps based on the distribution of this band's FWHM.

Figure 3 shows BSE images, CL images and hyperspectral PL maps of pairs of halves of heterogeneous zircon crystals, whereas one half is naturally radiation-damaged, the other one an-

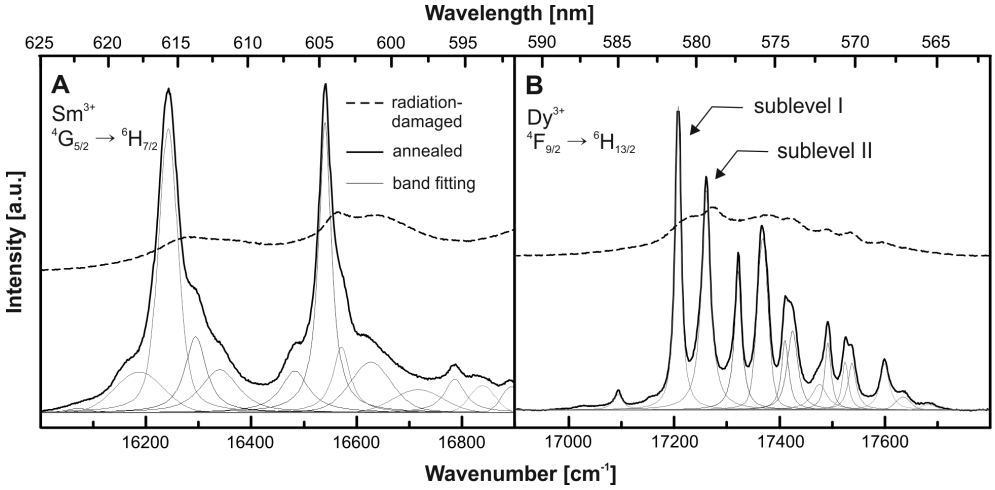

FIGURE 2. Pairs of PL spectra (λ_{exc} = 473 nm) obtained from the unannealed and annealed halves of zircon sample A1 (Adirondack Mts.). The two measurements were placed at corresponding locations, i.e., within the altered interior region of the crystal (cf. Fig. 3a). Spectra are shown with normalized maximum intensities and with vertical offset for clarity. (**A**) Emission related to the $^4G_{5/2} \rightarrow {}^6H_{7/2}$ transition of trace Sm^{3+}. (**B**) Emission related to the $^4F_{9/2} \rightarrow {}^6H_{13/2}$ transition of trace Dy^{3+}. Graphical results of least-square band fitting (assuming Lorentzian-Gaussian band shapes) are shown for spectra of annealed halves.

nealed. The PL maps show color-coded distribution patterns of the FWHM of sublevel I of the $^4F_{9/2} \rightarrow {}^6H_{13/2}$ transition of Dy^{3+}. Corresponding PL spectra and the respective Stark's levels used for mapping are presented in Figure 2B.

Figure 3 shows that accumulation of self-irradiation damage causes significant BSE increase and CL intensity decrease, as revealed by opposite trends upon structural reconstitution by dry annealing (Fig. 3). Nasdala et al. (2006) attempted to explain the BSE increase with increasing damage by electron channeling contrast (cf. Mitchell and Day 1998), and the CL-intensity loss upon damage accumulation was discussed by Nasdala et al. (2002). A similarly close, inverse correlation was observed also for the total PL emission, whose intensity decreases appreciably with increasing U concentration and radiation damage (see Fig. 2 again). The hypothesis that the presence of U is the main reason for the decreased PL emission (this effect was proposed for CL by Poller et al. 2001) is disproved by the fact that annealed halves have the same U concentrations as their unannealed counterparts but yield much more intense PL. Also, ion-irradiation of synthetic and natural zircon samples done by Finch et al. (2004) showed that REE^{3+} emissions observed in IL strongly decrease with increasing radiation damage. Finch et al. (2004) explained their observation by increasing defect concentrations upon increasing structural damage created, which give rise to non-radiative transitions and cause a reduced possibility of energy migration through the crystal.

In addition to the general intensity loss of PL bands increasing radiation damage results in clear increases in FWHMs of individual bands (see also, e.g., Nasdala et al. 2013). Hyperspectral PL maps (Fig. 3) show that in naturally radiation-damaged zircon, the FWHM of Dy^{3+} sublevel I is broadened particularly in zones with high uranium concentrations and, hence, with more extensive radiation damage. In contrast, zones with low uranium concentrations (with corresponding lower levels of accumulated radiation damage) are characterized by narrow Dy^{3+} Stark's level bands (for instance see overgrowth rim of sample 31E, Fig. 3c). Depending on the degree of radiation damage of particular interior regions, the Dy^{3+} sublevel near 17 200 cm^{-1} yielded FWHMs of up to >40 cm^{-1}, whereas predominantly values close to 12 cm^{-1} were obtained after annealing. Distribution patterns of the FWHM of certain REE-emission sublevels (here, Dy^{3+} sublevel I) are hence virtual distribution patterns of radiation damage or crystallinity, respectively.

It should be noted that, in contrast to FWHM or band position, the band intensity and intensity-related spectral parameters such as the area integral are not suitable to estimate directly the degree of disorder. This is because luminescence intensity strongly depends on further variables, such as the absolute concentration of the respective REE^{3+}, effects of quenching/sensitizing by other elements (e.g., Marfunin 1979; Kempe and Götze 2002), and effects of crystal orientation (e.g., Lenz et al. 2013). The present study was, hence, not focused merely on intensity-based REE distributions (e.g., MacRae et al. 2012, 2013), but based on the interpretation of band widths of REE emissions.

The dependence of the broadening of the PL emission on the structural damage, rather than on the U concentration, is supported by the observation that annealed halves (containing the same amounts of U as their unannealed counterparts; Table 1) show narrow Dy^{3+} sublevel-bands. Furthermore, clustering of REE centers potentially may also result in PL band broadening. The similarity of our PL maps and Raman maps for the same pairs of crystal-halves (presented by Nasdala et al. 2006) rather supports the dependence of PL broadening on the defect accumulation upon increasing radiation damage. Both show the very same distribution patterns, which are in the case of Raman maps caused predominantly by the radiation damage accumulated.

In addition to effects of structural damage on the PL broadening, however, minor effects of the chemical composition cannot be neglected. An example is the PL map in Figure 3a. The annealed half-zircon of sample A1 still shows a slightly heterogeneous FWHM distribution pattern. Nasdala et al. (2006) discussed their

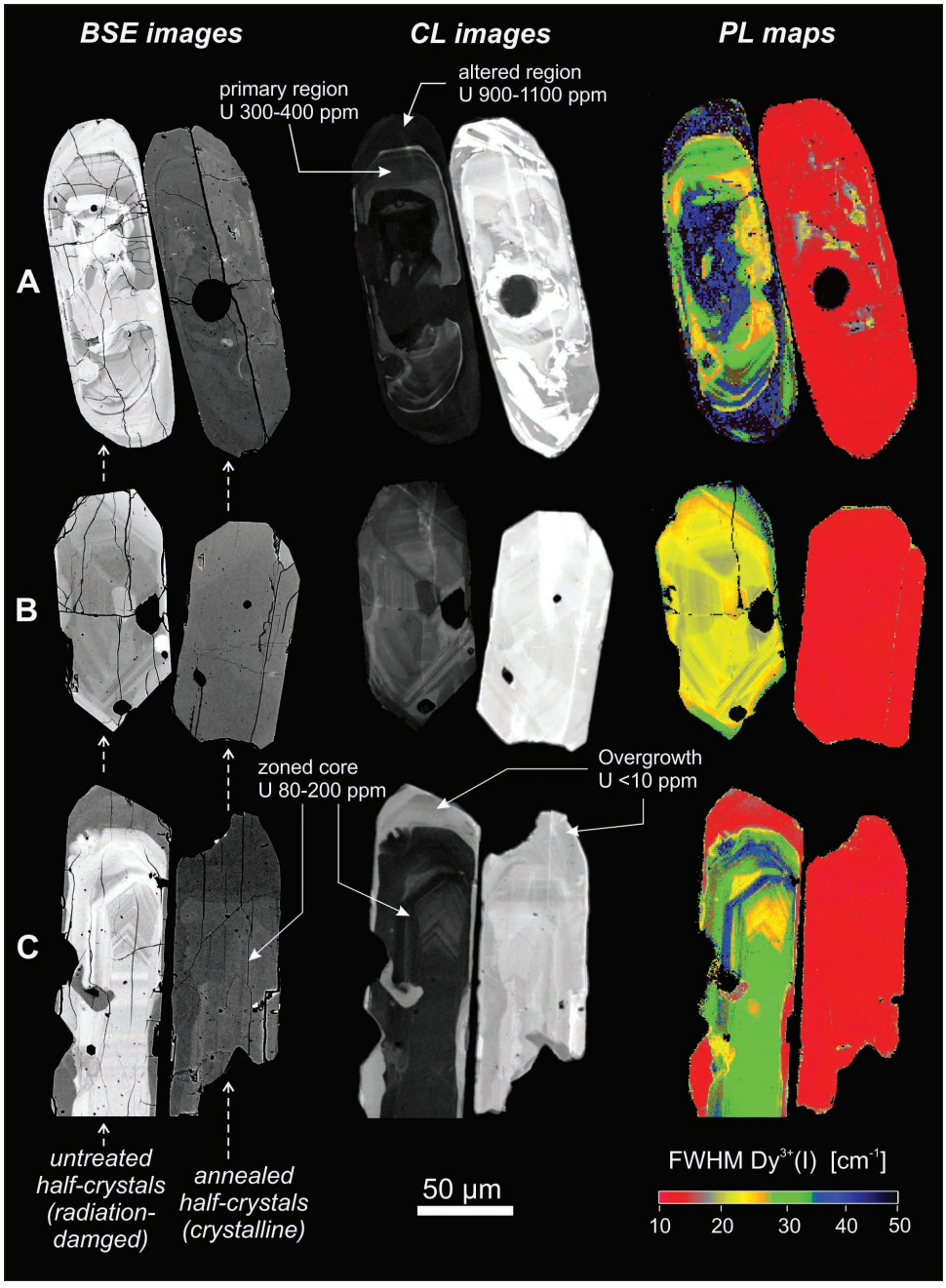

FIGURE 3. Images of cut zircon crystals from three different lithologies, with the heat-treated crystal half always shown in close proximity to its unannealed counterpart. (**a**) Zircon from a leucogranite, Adirondack Mountains, New York (sample A1). (**b**) Zircon from the Bluffpoint quartz diorite, Ontario (sample 81A). (**c**) Grain from the Mulcahy Lake intrusion, Ontario (sample 31E). In all three cases, a sequence of BSE and CL images (modified after Nasdala et al. 2006) and PL map is shown. The PL maps (λ_{exc} = 473 nm) were generated from the FWHM of the Dy^{3+} emission sublevel near 17200 cm^{-1} (sublevel I; compare Fig. 2).

similar Raman observation for the very same sample as possible indication of incomplete structural reconstitution during the heat treatment (four days at 1300 °C). As an alternative interpretation we consider the possibility that minor heterogeneity in their Raman map, and our PL map, may be due to minor heterogeneity of the chemical composition (i.e., FWHM increase due to the elevated presence of non-formula elements). These heterogeneous areas are characterized by slightly, but significantly, elevated concentrations of P_2O_5, REE_2O_3, and U/ThO_2 (see EPMA measurement point N3 from the sample A1 in Table 1).

The impact of compositional heterogeneity on the FWHM is supported also by the PL map of the very mildly radiation-damaged zircon M2 (Fig. 4), whose internal FWHM variations (between 14 and 25 cm^{-1} in the natural and between 12 and 15 cm^{-1} in the

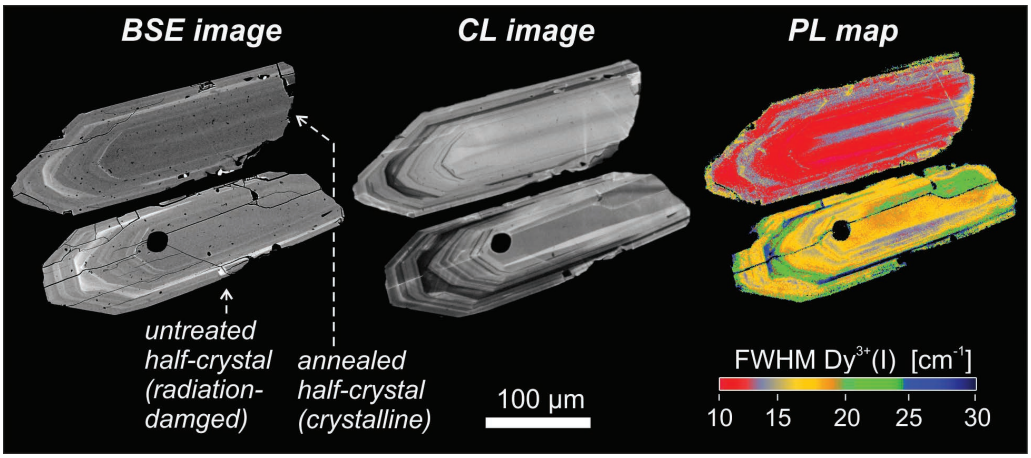

FIGURE 4. Series of BSE and CL image (modified after Nasdala et al. 2006) and PL map (λ_{exc} = 473 nm) of a cut zircon from a rhyolite tuff from the Gyulakeszi formation near Pécs, Hungary (sample M2). Note the different color-coding scale compared to the three PL maps in Figure 3. The non-uniformity of the BSE intensity within the annealed crystal half indicates that slight FWHM variations of the PL might be due to moderate chemically induced band broadening.

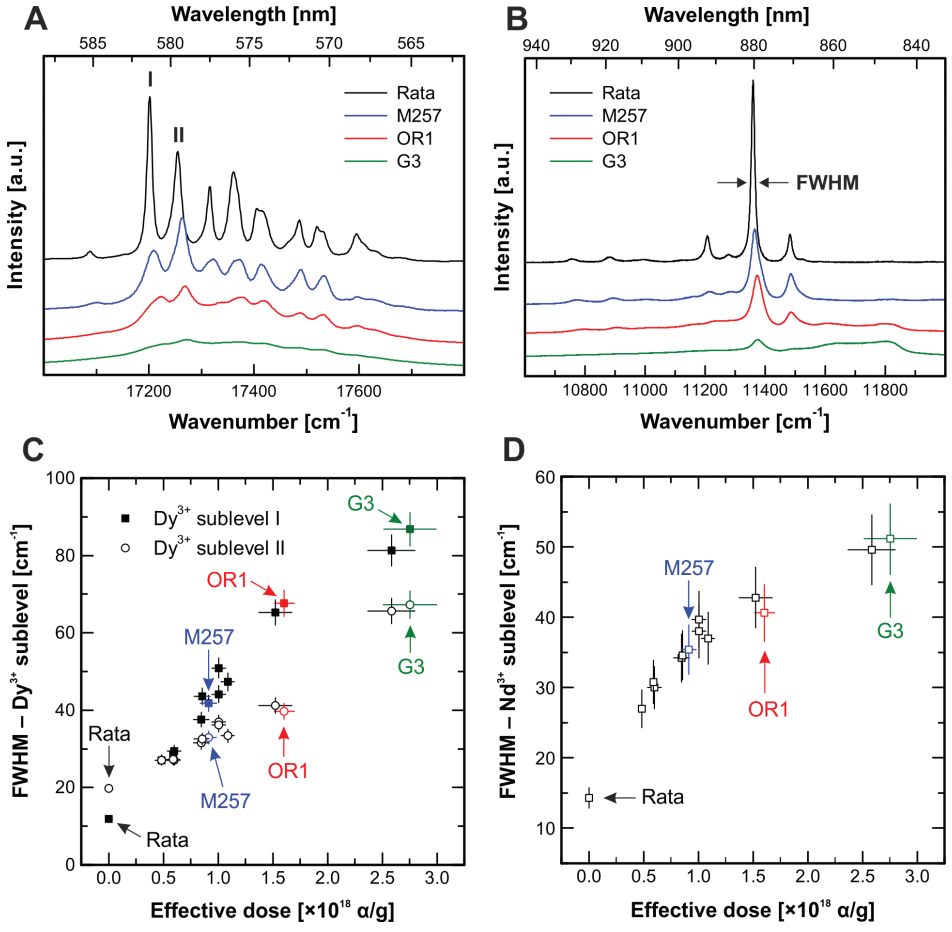

FIGURE 5. Effect of radiation damage on PL spectral parameters, obtained at room temperature, of gem-quality zircon samples. (**a** and **b**) Photoluminescence spectra (**a**, λ_{exc} = 473 nm; **b**, λ_{exc} = 532 nm) of samples whose degrees of radiation damage range from well crystalline (Rata) to severely damaged (G3). (**c**) Plot of the FWHM of two Dy^{3+} ($^4F_{9/2} \rightarrow {}^6H_{13/2}$) sublevels (which are indicated in **a**) against calculated effective α-doses. Note the clear FWHM-dose correlations, which however show different slopes. Data plotted were extracted from Table 1. (**d**) Plot of the FWHM of the ~11 350 cm^{-1} sublevel of Nd^{3+} ($^4F_{3/2} \rightarrow {}^4I_{9/2}$; marked in **b** with arrows) against calculated effective α-doses.

annealed half-crystal) are assigned in part to chemical heterogeneity. First, FWHMs are not uniform in the annealed crystal half (as it should be expected if FWHM broadening was solely due to structural damage). Second, the bright-BSE growth zone is characterized by both elevated concentrations of UO_2, ThO_2, and REE_2O_3 (Table 1) and the strongest PL band broadening (Fig. 4). Note that, due to its Neogene age (Harangi 2001), sample M2 has accumulated much less radiation damage compared to the zircon samples shown in Figure 3. Effects of radiation damage on the PL are hence less extensive in sample M2, and, correspondingly, the (minor) effects of the chemical composition on band FWHMs are detected because they are less obscured.

Effects of compositional-induced structural-disorder have been well documented already for the Nd^{3+} luminescence of monazite–(Ce) (e.g., PL study of Lenz et al. 2013). Note, however, that natural monazite–(Ce) typically has much higher compositional variability, when compared to natural zircon, which hence affects the FWHMs of PL emissions of monazite–(Ce) to much higher magnitudes. The impact of chemical heterogeneity on the FWHM of REE^{3+} Stark's levels in natural zircon is, therefore, comparably low.

Reference zircon spectra: Estimation of radiation damage

Effects of radiation damage on the Dy^{3+} and Nd^{3+} luminescence of zircon are visualized and determined more quantitatively by PL data obtained from a suite of gem-zircon samples from Ratnapura, Sri Lanka, and Ratanakiri, Cambodia (Fig. 5). Note that the Sri Lankan zircon samples represent various degrees of radiation damage, ranging from moderately (M144) to strongly damaged (G3; see Table 2; compare also Nasdala et al. 2004a). The Ratanakiri zircon, in contrast, is characterized by a remarkably low degree of self-irradiation damage (Wittwer et al. 2013), which is mainly due to the sample's young age of 1.2 ± 0.3 Ma (P.C. Piilonen, personal communication). Note also that the Sri Lanka zircon has experienced partial structural reconstitution in its geological history, which is why α-doses calculated based on the time period since the Neoproterozoic to Cambrian closure of the U–Pb system overestimate the radiation damage present (for details Nasdala et al. 2004a). To account for the annealing, "effective α-doses" were corrected applying a correction factor of 0.55 to the calculated total α-doses, as elucidated by Nasdala et al. (2004a).

In accordance to our findings described above, band widths of Dy^{3+} and Nd^{3+} luminescence sublevels show a marked increase that is closely related to the self-irradiation dose (Fig. 5). Note that the particular extent of the dose-related FWHM increase for a given Stark's level band is not necessarily uniform but may vary appreciably among emission centers and even among individual sublevels of a single transition. As an example, FWHMs of two sublevels belonging to the $^4F_{9/2} \rightarrow {}^6H_{13/2}$ transition of Dy^{3+} (labeled I and II in Fig. 5a), show divergent band-broadenings upon increasing α-doses (Fig. 5c). Dysprosium sublevel I [FWHM increase from 12 cm^{-1} (Rata) to 87 cm^{-1} (G3)] obviously is more sensitive to radiation-induced structural disorder, compared to Dy^{3+} sublevel II [FWHM increase from 20 cm^{-1} (Rata) to 68 cm^{-1} (G3)] and the ~11 350 cm^{-1} sublevel of Nd^{3+} ($^4F_{3/2} \rightarrow {}^4I_{9/2}$) [FWHM increase from 14 cm^{-1} (Rata) to 51 cm^{-1} (G3)], respectively (Fig. 5d). Consequently, for each single Stark's level that is intended to be used as measure of the radiation damage, a separate calibration of the FWHM-dose dependence needs to be available.

The FWHM increase of REE-related emissions in mildly to strongly radiation-damaged (but not yet fully amorphous) zircon is assigned to disturbance of the structure as caused by the accumulation of defects. These defects are considered to perturb the local crystallographic environment of the REE^{3+} centers. As a consequence, the crystal field around REE cations is distorted, and PL bands may shift slightly in spectral position. The spectral

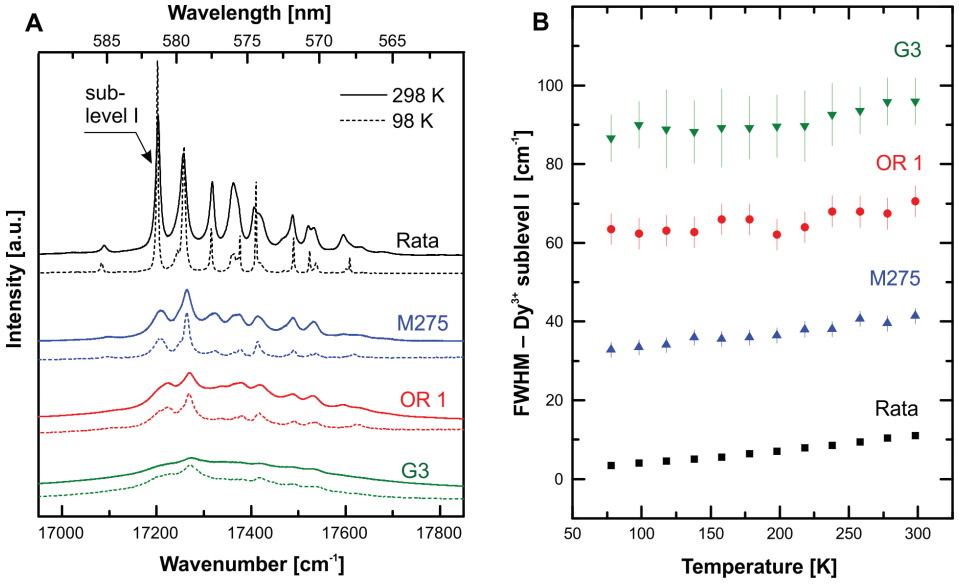

Figure 6. Effect of temperature on the PL spectra of various gem-quality zircon samples ranging from well crystallized to severely radiation damaged. (**a**) Pairs of spectra showing the Dy^{3+} emission ($^4F_{9/2} \rightarrow {}^6H_{13/2}$) at ambient and low temperature. (**b**) Plot of the FWHM of Dy^{3+} sublevel I (see arrow in **a**) against temperature. Note that FWHMs of Dy^{3+} Stark's levels depend strongly on the sample's degree of radiation damage (cf. Fig. 5), whereas temperature has moderate effects.

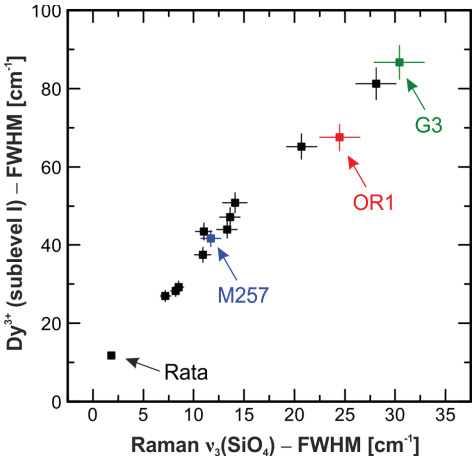

FIGURE 7. Plot of the FWHM of sublevel I of the Dy^{3+} $^4F_{9/2} \rightarrow {}^6H_{13/2}$ PL emission against the FWHM of the $\nu_3(SiO_4)$ Raman band (B_{1g} mode; antisymmetric stretching of SiO_4 tetrahedrons). Data pairs of the four gem-quality zircon samples, whose PL spectra are shown in Figure 5, are labeled and marked with arrows.

band detected may then be regarded as superposition of a multitude of single levels arising from variably distorted crystallographic sites within the spatially resolved area analyzed (e.g., Skinner and Moerner 1996; Lenz et al. 2013).

Completely metamict $ZrSiO_4$, and amorphous volumes in moderately damaged zircon, are in contrast characterized by randomly perturbed cation sites, which results in the entire degeneration of REE^{3+} crystal-field states. This in turn leads to the total loss of fine structure of electronic transitions, i.e., no more distinct Stark's levels but broad single bands are observed in PL spectra. Analogous effects are observed in PL spectra of glasses produced by melt quenching; see for instance the PL spectra of Dy-doped $CaTiSiO_5$ glass (degenerate transitions) and crystal (Stark fine-split transitions) in Figure 15 of Nasdala et al. (2004b). Consequently, the broadened (but still split) Stark's level bands obtained from zircon samples studied here are assigned to the crystalline fraction present, whereas amorphous clusters (for a general description of the damage-accumulation process see Murakami et al. 1991) are virtually "PL-invisible" at low self-irradiation doses. At elevated radiation damage, fitting of individual Stark's level bands is feasible as long as a minimum of remnant (even though strongly stressed) crystalline volume units contribute to the luminescence emission, and provided the REE signal originating from the amorphous volume fraction does not hamper too much the background.

Note, however, that FWHMs of luminescence bands also depend on temperature. In general, low-temperature luminescence studies are conducted to improve the sharpness of individual bands (for the narrowing of REE^{3+} emissions at low temperatures see, e.g., Reisfeld and Jørgensen 1977; Marfunin 1979; Blasse and Grabmaier 1994; Lenz et al. 2013). Figure 6a shows an exemplary low-temperature series of PL spectra of Dy^{3+} in zircon samples representing various degrees of radiation damage. The plot of FWHMs against temperature (Fig. 6b) however indicates that FWHMs of Dy^{3+} sublevels differ appreciably among variably radiation-damaged samples. In contrast, the effect of temperature on the FWHMs (i.e., narrowing with lowered temperature) is comparably low. The band FWHMs decrease by approximately about –8 cm^{-1} from ambient temperature to 78 K (virtually independent from the degree of the sample's radiation damage).

The effect of temperature on widths of REE^{3+} emissions (i.e., 4*f* elements) is hence comparatively small when compared with *d-d* or *d-f* transitions. This is because *f*-electrons and their inter-transitions are well shielded by the outermost filled $5s^25p^6$ orbitals (Blasse and Grabmaier1994). Low-temperature PL measurements are, therefore, of insignificant usefulness to increase the reliability of FWHM estimates for strongly radiation-damaged zircon (see data for samples OR1 and G3 in Fig. 6b). The effective temperature-induced narrowing of Stark's levels of these two samples does not exceed significantly the statistical error of the FWHM estimates. In addition, low-temperature measurements performed by using cooling stages or other liquid-nitrogen setups entail considerable effort; especially for measurements with high lateral resolution such as for hyperspectral PL mapping. Therefore, all reference luminescence spectra presented in the sections above are recorded at room temperature (298 K) as this study promotes the application of REE^{3+} luminescence spectroscopy being used potentially for various other techniques as well (such as CL coupled to EPMA). Nevertheless, for unbiased quantitative estimates, it needs to be ensured that luminescence analyses are done at room temperature or, alternatively, at the same temperature as the calibration measurements. Consequently, uncontrolled sample heating, such as due to intense local absorption of the incident laser light, must be avoided.

IMPLICATIONS

The REE^{3+} luminescence of zircon was found once again to be very sensitive to structural disorder caused by corpuscular self-irradiation. The emission intensity generally decreases, and band FWHMs increase, possibly accompanied by minor band shifts, with increasing structural damage. Our results show that the band-widths of distinct sublevels of Dy^{3+} ($^4F_{9/2} \rightarrow {}^6H_{13/2}$) and Nd^{3+} ($^4F_{3/2} \rightarrow {}^4I_{9/2}$) emissions (1) can be determined reliably by conventional band-fitting procedures and (2) is strongly related to the amount of radiation-damage accumulated (the latter being expressed by the effective time-integrated α-dose; Fig. 5). We propose the use of the FWHM of the Stark's level at ~17 200 cm^{-1} of the $^4F_{9/2} \rightarrow {}^6H_{13/2}$ transition of Dy^{3+} (here described as sublevel I; see again Fig. 5c) and the dominant Stark's level of Nd^{3+} near 11 350 cm^{-1} (Figs. 5b and 5d) as most suitable means of estimating quantitatively the radiation-induced structural disorder of zircon on a micrometer-scale.

Estimation of the crystallinity based on REE-band FWHMs may open up new opportunities to characterize the structural state of radiation-damaged zircon, complementary to the use of Raman-band FWHMs for this purpose (Nasdala et al. 1995, 2001). This is supported by Figure 7, which shows that the radiation-damage induced FWHM increase of the Dy^{3+} sublevel I is related to that of the $\nu_3(SiO_4)$ Raman band of zircon. Potential advantages of using REE^{3+} luminescence spectroscopy include (1) the high-volume resolution (with confocal spectrometer systems, analyses can be done on a micrometer scale), (2) the

option to do non-destructive analyses without sample preparation, and (3) the possibility to obtain the FWHM of Stark's levels of multiple REE^{3+} centers simultaneously (e.g., Dy^{3+} and Nd^{3+}). The latter (i.e., choosing another center or transition) may be advisable if a Stark's level under analysis should be obscured by other phenomena (e.g., defect-related broad-band emissions created upon corpuscular irradiation; Götze et al. 1999; Finch et al. 2004; Nasdala et al. 2013). The proposed PL of Dy^{3+} sublevel I may be used widely in studying zircon, because according to our experience, trace-Dy is virtually omnipresent in natural zircon, and even minute quantities yield well-measurable luminescence signals. Finally, similar to FWHMs of SiO_4-related Raman bands, FWHMs of the Dy^{3+} (and Nd^{3+}) signals studied here were found to depend predominantly on the degree of radiation damage present, whereas chemical effects, which may be much more extensive in minerals that typically are compositionally variable, are almost negligible in the case of (unaltered igneous or metamorphic) zircon.

Acknowledgments

Thanks to D.W. Davis, D. Frei, J.M. Hanchar, W. Hofmeister, A.K. Kennedy, I. Oláh, P. Piilonen, R. Stern, D. Talla, B. Wanthanachaisaeng, and M.J. Whitehouse for providing samples and/or data. Sample preparation was done by D. Dettmar, M. Tichomirowa, and A. Wagner. Critical comments of Adrian Finch and two anonymous reviewers are gratefully acknowledged. Financial support was provided by the Materials Science Research Centre, Mainz, Germany, and the Austrian Science Fund (FWF), grant P24448–N19 to L.N.

References cited

Balan, E., Neuville, D.R., Trocellier, P., Fritsch, E., Muller, J.P., and Calas, G. (2001) Metamictization and chemical durability of detrital zircon. American Mineralogist, 86, 1025–1033.

Blanc, P., Baumer, A., Cesbron, F., Ohnenstetter, D., Panczer, G., and Rémond, G. (2000) Systematic cathodoluminescence spectral analysis of synthetic doped minerals: anhydrite, apatite, calcite, fluorite, scheelite and zircon. In M. Pagel, V. Barbin, P. Blanc, and D. Ohnenstetter, Eds., Cathodoluminescence in Geosciences, 127–160. Springer, Berlin.

Brøgger, W.C. (1893) Amorf: Salmonens store illustrerede Konversationslexikon, 1, 742–743.

Burns, R.G. (1993) Mineralogical applications of crystal field theory. Cambridge Topics in Mineral Physics and Chemistry, 5, Cambridge University Press.

Blasse, G., and Grabmaier, B. (1994) Luminescence Materials, 248 p., Springer, Berlin.

Cesbron, F., Blanc, P., Ohnenstetter, D., and Rémond, G. (1995) Cathodoluminescence of rare earth doped zircons. I. Their possible use as reference materials. Scanning Microscopy Supplement, 9, 35–56.

Chakoumakos, B.C., Oliver, B.C., Lumpkin, G.R., and Ewing, R.C. (1991) Hardness and elastic modulus of zircon as a function of heavy-particle irradiation dose. I. In situ a-decay event damage. Radiation Effects and Defects in Solids, 118, 393–403.

Corfu, F., Hanchar, J.M., Hoskin, P.W.O., and Kinny, P. (2003) Atlas of zircon textures. In J.M. Hanchar and P.W.O. Hoskin, Eds., Zircon, 53, p. 469–500. Reviews in Mineralogy and Geochemistry, Mineralogical Society of America, Chantilly, Virginia.

Davis, D.W., and Edwards, G.R. (1985) The petrogenesis and metallogenesis of the Atikwa-Lawrence volcanic-plutonic terrain. Grant 179, Ontario Geological Survey Miscellaneous Publication, 127, 101–111.

Deliens, M., Delhal, J., and Tarte, P. (1977) Metamictization and U-Pb systematics – a study by infrared absorption spectrometry of Precambrian zircons. Earth and Planetary Science Letters, 33, 331–344.

Dieke, G.H., and Crosswhite, H.M. (1963) The spectra of the doubly and triply ionized rare earths. Applied Optics, 2, 675–686.

Ewing, R.C. (1993) The metamict state: 1993—the centennial. Nuclear Instruments and Methods in Physics Research Section B, 91, 22–29.

——— (2001) The design and evaluation of nuclear-waste forms: clues from mineralogy. Canadian Mineralogist, 39, 697–715.

Farnan, I., and Salje, E.K.H. (2001) The degree and nature of radiation damage in zircon observed by ^{29}Si nuclear magnetic resonance. Journal of Applied Physics, 89, 2084–2090.

Farnan, I., Cho, H., and Weber, W.J. (2007) Quantification of actinide α-radiation damage in minerals and ceramics. Nature, 445, 190–193.

Finch, R.J., Hanchar, J.M., Hoskin, P.W.O., and Burns, P.C. (2001) Rare-earth elements in synthetic zircon: Part 2. A single-crystal X-ray study of xenotime substitution, American Mineralogist, 86, 681–689.

Finch, A.A., Garcia-Guinea, J., Hole, D.E., Townsend, P.D., and Hanchar, J.M. (2004) Ionoluminescence of zircon: rare earth emissions and radiation damage. Journal of Physics D, 2795–2803.

Friis, H., Finch, A.A., Williams, C.T., and Hanchar, J.M. (2010) Photoluminescence of zircon ($ZrSiO_4$) doped with REE^{3+} (REE= Pr, Sm, Eu, Gd, Dy, Ho, Er). Physics and Chemistry of Minerals, 37, 333–342.

Gaft, M., Panczer, G., Reisfeld, R., and Uspensky, E. (2001) Laser-induced time-resolved luminescence as a tool for rare-earth element identification in minerals. Physics and Chemistry of Minerals, 28, 347–363.

Geisler, T., Trachenko, K., Ríos, S., Dove, M.T., and Salje, E.K.H. (2003a) Impact of self-irradiation damage on the aqueous durability of zircon ($ZrSiO_4$): implications for its suitability as a nuclear waste form. Journal of Physics: Condensed Matter, 15, 597–605.

Geisler, T., Pidgeon, R.T., Kurtz, R., van Bronswijk, W., and Schleicher, H. (2003b) Experimental hydrothermal alteration of partially metamict zircon. American Mineralogist, 88, 1496–1513.

Geisler, T., Burakov, B., Zirlin, V., Nikolaeva, L., and Pöml, P. (2005) A Raman spectroscopic study of high-uranium zircon from the Chernobyl "lava". European Journal of Mineralogy, 17, 883–894.

Götze, J. (2000) Cathodoluminescence microscopy and spectroscopy in applied mineralogy. Freiberger Forschungsheft C 485, TU Bergakademie Freiberg, 128 p.

——— (2002) Potential of cathodoluminescence (CL) microscopy and spectroscopy for the analysis of minerals and materials. Analytical and Bioanalytical Chemistry, 374, 703–708.

Götze, J., Kempe, U., Habermann, D., Nasdala, L., Neuser, R.D., and Richter, D.K. (1999) High-resolution cathodoluminescence combined with SHRIMP ion probe measurements of detrital zircons. Mineralogical Magazine, 63, 179–187.

Götze, J., Schertl, H.P., Neuser, R.D., Kempe, U., and Hanchar, J.M. (2013) Optical microscope-cathodoluminescence (OM–CL) imaging as a powerful tool to reveal internal textures of minerals. Mineralogy and Petrology, 107, 373–392.

Hanchar, J.M., and Miller, C.F. (1993) Zircon zonation patterns as revealed by cathodoluminescence and backscattered electron images: implications for interpretation of complex crustal histories. Chemical Geology, 110, 1–13.

Hanchar, J.M., and Rudnick, R.L. (1995) Revealing hidden structures: the application of cathodoluminescence and back-scattered electron imaging to dating zircons from lower crustal xenoliths. Lithos, 36, 289–303.

Hanchar, J.M., Finch, R.J., Hoskin, P.W.O., Watson, E.B., Cherniak, D.J., and Mariano, A.M. (2001) Rare earth elements in synthetic zircon: part 1. Synthesis, and rare earth element and phosphorus doping. American Mineralogist, 86, 667–680.

Harangi, S. (2001) Neogene to Quarternary volcanism of the Carpathian-Pannonian region—a review. Acta Geologica Hungarica, 44, 223–258.

Holland, H.D., and Gottfried, D. (1955) The effect of nuclear radiation on the structure of zircon. Acta Crystallographica, 8, 291–300.

Jazmati, A.K., and Townsend, P.D. (2000) Photoluminescence from RE doped BGO waveguides. Nuclear Instruments and Methods in Physics Research Section B: Beam Interactions with Materials and Atoms, 166, 597–601.

Karali, T., Can, N., Townsend, P.D., Rowlands, A.P., and Hanchar, J.M. (2000) Radioluminescence and thermoluminescence of rare earth element and phosphorus-doped zircon. American Mineralogist, 85, 668–681.

Kempe, U., and Götze, J. (2002) Cathodoluminescence (CL) behaviour and crystal chemistry of apatite from rare-metal deposits. Mineralogical Magazine, 66, 151–172.

Kempe, U., Gruner, T., Nasdala, L., and Wolf, D. (2000) Relevance of cathodoluminescence for interpretation of U-Pb zircon ages (with an example of application to a study of zircons from the Saxonian Granulite Complex, Germany). In M. Pagel, V. Barbin, P. Blanc, and D. Ohnenstetter, Eds., Cathodoluminescence in Geosciences, p. 415–455. Springer, Berlin.

Lenz, C., Talla, D., Ruschel, K., Skoda, R., Götze, J., and Nasdala, L. (2013) Factors affecting the Nd^{3+} (REE^{3+}) luminescence of minerals. Mineralogy and Petrology, 107, 415–428.

MacRae, C.M., Wilson, N.C., Torpy, A., and Davidson, C.J. (2012) Hyperspectral cathodoluminescence imaging and analysis extending from ultraviolet to near infrared. Microscopy and Microanalysis, 18, 1239–1245.

MacRae, C.M., Wilson, N.C., and Torpy, A. (2013) Hyperspectral cathodoluminescence. Mineralogy and Petrology, 107, 429–440.

Mariano, A.N. (1989) Cathodoluminescence emission spectra of rare earth element activators in minerals. In B.R. Lipin and G.A. McKay, Eds., Geochemistry and Mineralogy of Rare Earth Elements, p. 339–348. Reviews in Mineralogy, 21, Mineralogical Society of America, Chantilly, Virginia.

Marfunin, A.S. (1979) Spectroscopy, Luminescence, and Radiation Centers in Minerals, 352 p. Springer, Berlin.

Mathieu, R., Zetterström, L., Cuney, M., Gauthier-Lafaye, F., and Hidaka, H. (2001) Alteration of monazite and zircon and lead migration as geochemical tracers of fluid paleocirculations around the Oklo–Okélobondo and Bangombé natural nuclear reaction zones (Franceville basin, Gabon). Chemical Geology, 171, 147–171.

McLelland, J., Morrison, J., Selleck, B., Cunningham, B., Olson, C., and Schmidt, K. (2001) Hydrothermal alteration of late- to post-tectonic Lyon Mountain granitic gneiss, Adirondack Highlands, New York: Origin of quartz-sillimanite segregations, quartz-albite lithologies, and associated Kiruna-type low-Ti Fe-oxide deposits. Journal of Metamorphic Geology, 19, 1–19.

Mitchell, D.R.G., and Day, R.A. (1998) Electron channelling contrast imaging of defect structures in neutron irradiated aluminium. Scripta Materialia, 39, 923–930.

Morrison, D.A., Davis, D.W., Wooden, J.L., Bogard, D.D., Maczuga, D.E., Phinney, W.C., and Ashwal, L.D. (1985) Age of the Mulcahy Lake intrusion, northwest Ontario, and implications for the evolution of greenstone-granite terraines. Earth and Planetary Science Letters, 73, 306–316.

Murakami, T., Chakoumakos, B.C., Ewing, R.C., Lumpkin, G.R., and Weber, W.J. (1991) Alpha-decay event damage in zircon. American Mineralogist, 76, 1510–1532.

Nasdala, L., Wolf, D., and Irmer, G. (1995) The degree of metamictization in zircon: a Raman spectroscopic study. European Journal of Mineralogy, 7, 471–478.

Nasdala, L., Wenzel, M., Vavra, G., Irmer, G., Wenzel, T., and Kober, B. (2001) Metamictisation of natural zircon: accumulation versus thermal annealing of radioactivity-induced damage. Contributions to Mineralogy and Petrology, 141, 125–144.

Nasdala, L., Lengauer, C.L., Hanchar, J.M., Kronz, A., Wirth, R., Blanc, P., Kennedy, A.K., and Seydoux-Guillaume, A.-M. (2002) Annealing radiation damage and the recovery of cathodoluminescence. Chemical Geology, 191, 121–140.

Nasdala, L., Reiners, P.W., Garver, J.I., Kennedy, A.K., Stern, R.A., Balan, E., and Wirth, R. (2004a) Incomplete retention of radiation damage in zircon from Sri Lanka. American Mineralogist, 89, 219–231.

Nasdala, L., Götze, J., Hanchar, J.M., Gaft, M., and Krbetschek, M.R. (2004b) Luminescence techniques in Earth sciences. In A. Beran and E. Libowitzky, Eds., Spectroscopic Methods in Mineralogy, 6, 43–91. EMU Notes in Mineralogy, Eötvös University Press, Budapest.

Nasdala, L., Kronz, A., Hanchar, J.M., Tichomirowa, M., Davis, D.W., and Hofmeister, W. (2006) Effects of natural radiation damage on back-scattered images of single crystals of minerals. American Mineralogist, 91, 1739–1746.

Nasdala, L., Hofmeister, W., Norberg, N., Martinson, J.M., Corfu, F., Dörr, W., Karno, S.L., Kennedy, A.K., Kronz, A., Reiners, P.W., and others. (2008) Zircon M257—A homogeneous natural reference material for the ion microprobe U-Pb analysis of zircon. Geostandards and Geoanalytical Research, 32, 247–265.

Nasdala, L., Beyssac, O., Schopf, J. W., and Bleisteiner, B. (2012) Application of Raman-based images in the Earth sciences. In A. Zoubir, Ed., Raman Imaging—Techniques and applications, 145–187. Springer Series in Optical Sciences, 168, Springer, Berlin.

Nasdala, L., Grambole, D., and Ruschel, K. (2013) Review of effects of radiation damage on the luminescence emission of minerals, and the example of He-irradiated $CePO_4$. Mineralogy and Petrology, 107, 441–454.

Nicholas, J.V. (1967) Origin of the luminescence in natural zircon. Nature, 215, 1476.

Ollier, N., Concas, G., Panczer, G., Champagnon, B., and Charpentier, T. (2003) Structural features of a Eu^{3+} doped nuclear glass and gels obtained from glass leaching. Journal of Non-Crystalline Solids, 328, 207–214.

Pabst, A. (1952) The metamict state. American Mineralogist, 37, 137–157.

Palenik, C.S., Nasdala, L., and Ewing, R.C. (2003) Radiation damage in zircon. American Mineralogist, 88, 770–781.

Panczer, G., De Ligny, D., Mendoza, C., Gaft, M., Seydoux-Guillaume, A., and Wang, X. (2012) Raman and fluorescence. In J. Dubessy, M.-C. Caumon, and F. Rull, Eds., Applications of Raman Spectroscopy to Earth Sciences and Cultural Heritage, 12, p. 61–82. EMU Notes in Mineralogy, Eötvös University Press, Budapest.

Poller, U., Huth, J., Hoppe, P., and Williams, I.S. (2001) REE, U, Th, and Hf distribution in zircon from Western Carpathian Variscan granitoids: A combined cathodoluminescence and ion microprobe study. American Journal of Science, 301, 858–876.

Rakovan, J., and Reeder, R.J. (1996) Intracrystalline rare earth element distributions in apatite: surface structural influences on incorporation during growth. Geochimica et Cosmochimica Acta, 60, 4435–4445.

Reisfeld, R., and Jørgensen, C.H. (1977) Lasers and Excited States of Rare Earths. Inorganic Chemistry Concepts, 1, Springer, Berlin.

Reisfeld, R., Zigansky, E., and Gaft, M. (2004) Europium probe for estimation of site symmetry in glass films, glasses and crystals. Molecular Physics, 102, 1319–1330.

Rémond, G., Cesbron, F., Chapoulie, R., Ohnenstetter, D., Roques-Carmes, C., and Schoverer, M. (1992) Cathodoluminescence applied to the microcharacterization of mineral materials: a present status in experimentation and interpretation. Scanning Microscopy, 6, 23–68.

Ríos, S., Salje, E.K., Zhang, M., and Ewing, R.C. (2000) Amorphization in zircon: evidence for direct impact damage. Journal of Physics: Condensed Matter, 12, 2401–2412.

Rubin, J.N., Henry, C.D., and Price, J.G. (1989) Hydrothermal zircons and zircon overgrowths, Sierra Blance Peaks, Texas. American Mineralogist, 74, 865–869.

Ruschel, K., Nasdala, L., Rhede, D., Wirth, R., Lengauer, C.L., and Libowitzky, E. (2010) Chemical alteration patterns in metamict fergusonite. European Journal of Mineralogy, 22, 425–433.

Skinner, J., and Moerner, W. (1996) Structure and dynamics in solids as probed by optical spectroscopy. Journal of Physical Chemistry, 100, 13251–13262.

Ternane, R., Ferid, M., Panczer, G., Trabelsi-Ayadi, M., and Boulon, G. (2005) Site-selective spectroscopy of Eu^{3+}-doped orthorhombic lanthanum and monoclinic yttrium polyphosphates. Optical Materials, 27, 1832–1838.

Törnroos, R. (1985) Metamict zircon from Mozambique. Bulletin of the Geological Society of Finland, 57, 181–195.

Van Es, H.J., Vainshtein, D.I., Rozendaal, A., Donoghue, J.F., De Meijer, R.J., and Den Hartog, H.W. (2002) Thermoluminescence of $ZrSiO_4$ (zircon): A new dating method?. Nuclear Instruments and Methods in Physics Research Section B: Beam Interactions with Materials and Atoms, 191, 649–652.

Vavra, G. (1990) On the kinematics of zircon growth and its petrogenetic significance: a cathodoluminescence study. Contributions to Mineralogy and Petrology, 106, 90–99.

Vaz, J.E., and Senftle, F.E. (1971) Thermoluminescence study of the natural radiation damage in zircon. Journal of Geophysical Research, 76, 2038–2050.

Wasilewski, P.J., Senftle, F.E., Vaz, J.E., Thorpe, A.N., and Alexander, C.C. (1973) A study of the natural α-recoil damage in zircon by infrared spectra. Radiation Effects, 17, 191–199.

Weber, W.J. (1990) Radiation-induced defects and amorphization in zircon. Journal of Materials Research, 5, 2687–2697.

Wegh, R.T., Meijerink, A., Lamminmäki, R.J., and Hölsä, J. (2000) Extending Dieke's diagram. Journal of Luminescence, 87, 1002–1004.

Wittwer, A., Nasdala, L., Wanthanachaisaeng, B., Bunnag, N., Skoda, R., Balmer, W. A., Giester, G., and Zeug, M. (2013) Mineralogical characterisation of gem zircon from Ratanakiri, Cambodia. In CORALS–2013: Conference on Raman and Luminescence Spectroscopy in the Earth Sciences, Vienna, Austria, July 3–6 (2013) Book of abstracts, p. 115–116, http://www.univie.ac.at/Mineralogie/Corals2013/abstracts.html.

Yang, B., Luff, B.J., and Townsend, P.D. (1992) Cathodoluminescence of natural zircons. Journal of Physics: Condensed Matter, 4, 5617–5624.

Yang, C., Homman, N.O., Johansson, L., and Malmqvist, K.G. (1994) Microcharacterizing zircon mineral grain by ionoluminescence combined with PIXE. Nuclear Instruments and Methods in Physics Research Section B: Beam Interactions with Materials and Atoms, 85, 808–814.

Zhang, M., and Salje, E.K. (2001) Infrared spectroscopic analysis of zircon: Radiation damage and the metamict state. Journal of Physics: Condensed Matter, 13, 3057–3071.

Zhang, M., Boatner, L.A., Salje, E.K., Ewing, R.C., Daniel, P., Weber, W.J., Zhang, Y., and Farnan, I. (2008) Micro-Raman and micro-infrared spectroscopic studies of Pb-and Au-irradiated $ZrSiO_4$: Optical properties, structural damage, and amorphization. Physical Review B, 77(14), 144110.

Manuscript received January 21, 2014
Manuscript accepted December 1, 2014
Manuscript handled by Callum Hetherington